2011

Parametric Study on Instabilities in a Two-Layer Electromagnetohydrodynamic Channel Flow Confined Between Two Parallel Electrodes

P. Dinesh Sankar Reddy

Dipankar Bandyopadhyay

Sang Woo Joo

Ashutosh Sharma

Shizhi Qian
Old Dominion University, sqian@odu.edu

Original Publication Citation

Reddy, P. D. S., Bandyopadhyay, D., Joo, S. W., Sharma, A., & Qian, S. (2011). Parametric study on instabilities in a two-layer electromagnetohydrodynamic channel flow confined between two parallel electrodes. *Physical Review E, 83*(3), 036313. doi:10.1103/PhysRevE.83.036313

Parametric study on instabilities in a two-layer electromagnetohydrodynamic channel flow confined between two parallel electrodes

P. Dinesh Sankar Reddy,[1] Dipankar Bandyopadhyay,[2] Sang Woo Joo,[3,*] Ashutosh Sharma,[1,3,†] and Shizhi Qian[3,4]

[1]*Department of Chemical Engineering, Indian Institute of Technology Kanpur, Kanpur 208016, India*

[2]*Department of Chemical Engineering, Indian Institute of Technology Guwahati, Assam 781039, India*

[3]*School of Mechanical Engineering, Yeungnam University, Gyongsan 712-749, South Korea*

[4]*Department of Mechanical and Aerospace Engineering, Old Dominion University, Norfolk, Virginia 23529, USA*

(Received 31 October 2010; revised manuscript received 14 January 2011; published 22 March 2011)

Instabilities in a two-phase electromagnetohydrodynamic (EMHD) flow between a pair of parallel electrodes are explored. A linear stability analysis has been performed based on a coupled Orr-Sommerfeld system generated from the conservation laws. The study shows the presence of a finite-wave-number EMHD mode of instability in addition to the two commonly observed instability modes in the pressure-driven two-layer flows, namely, the long-wave interfacial mode arising from the viscosity or density stratification and the finite-wave-number shear flow mode engendered by the Reynolds stresses. This extra EMHD mode originates from the additional stresses generated by the Lorenz force acting at the liquid layers and is found to exist under all conditions beyond a critical strength of the externally applied magnetic field. The EMHD mode either can exist as a singular dominant mode or can coexist as a dominant or subdominant mode with the conventional interfacial mode or shear flow instabilities in the two-layer flows. The EMHD flow studied here has numerous potential applications in fluid transport, enhanced heat and mass transfer, mixing, and emulsification because of the low energy requirement, flow reversibility, absence of moving parts, and facile control over flow rate. The parametric study presented here on the instabilities in the two-layer EMHD flow will thus be of great practical use.

DOI: 10.1103/PhysRevE.83.036313 PACS number(s): 47.65.−d, 47.55.−t, 47.20.Ma

I. INTRODUCTION

Transport of highly conducting fluids on the macroscopic scale employing the Lorenz force has been conventionally utilized since the early report of Ritchie [1]. Recent studies show that magnetohydrodynamic (MHD) flows can also be a viable option for transporting weakly conducting fluids in microscale systems, such as flow inside the microchannel networks of a lab-on-a-chip device [2–6]. In microfluidic devices multiple fluids may be transported through a channel for various reasons. For example, increase in mobility of a fluid may be achieved by stratification of a highly mobile fluid or mixing of two or more fluids in transit may be designed for emulsification or heat and mass transfer applications. In that regard, magnetic-field-driven micropumps are in increasing demand due to their long-term reliability in generating flow, absence of moving parts, low power requirement, flow reversibility, feasibility of buffer solution manipulation, and mixing efficiency [7–13]. MHD flows inside channels can be propelled in many different ways, for example, in electromagnetohydrodynamics (EMHD) axial flow along a channel is generated by the interaction between the magnetic field and an electric field acting normal to it [1,4,5] as shown schematically in Fig. 1. Regardless of the purpose of a multifluid EMHD flow, it is important to understand the dynamics of interfaces between the fluids and its effect on the transport characteristics of the system. In the present study, for a fundamental understanding of such dynamics, we examine the stability of two immiscible fluid layers driven by the Lorenz force through a micro Hele-Shaw cell.

The stability of conventional Poiseuille or Couette flows of two superposed viscous fluids has been studied by numerous investigators, as summarized in the reviews [14–16]. In a pioneering analysis, Yih [17] showed that the pressure-driven two-layer plane Poiseuille flow (PPF) and Couette flow can develop long-wave instability of the interfacial mode. Hickox [18] later showed that an interfacial mode can also appear due to density stratification in pipe flows, whereas Smith and Davis [19] confirmed the presence of the interfacial mode under imposed shear. A few subsequent studies [20–23] showed that the long-wave interfacial mode can also exist in two-layer Couette flow when the thinner layer is more viscous. The finite-wave-number shear mode of instability in two-fluid Couette flow was first reported by Hooper and Boyd [24]. The origin of the shear mode is attributed to the destabilizing Reynolds stresses [25,26]. Yiantsios and Higgins [27] later extended Yih's [17] work to arbitrary flow properties, wave numbers, and volume fractions to show that the hydrostatic effects can suppress the interfacial mode by reducing the viscosity stratification, and provided further insights into the experimental observations of Kao and Park [28]. Later it was concluded that in the absence of gravity a two-layer plane Poiseuille flow is neutrally stable when $\mu_r = d_r^2$ due to the fading shear rate of the base flow at the interface, where μ_r and d_r are the viscosity and the thickness ratio, respectively [27,29]. In general, macroscopic pressure-driven two-layer flows inside rectangular channels are generated by means of pumps or stirrers. Recent technological trends show that the use of external fields to generate flow and instabilities inside channels, such as electrohydrodynamic [30–38], MHD [1,13,39,45], and electrokinetic [46–49] flows, can be more advantageous in many microscale applications.

*swjoo@ynu.ac.kr,
†ashutos@iitk.ac.in

Stability analysis of two-fluid EMHD flows has received attention in a somewhat different context due to its importance in a conventional application, the aluminum (Al) reduction cell. Al is produced from a solution of alumina in molten cryolite between two horizontal planar carbon electrodes with separation much smaller than their horizontal dimension. An applied vertical electric current heats the solution, which divides into two horizontal layers, cryolite on the top and liquid Al on the bottom. A vertical magnetic field is applied as well due to currents outside the cell. The stability analysis predicts instability of the interface when the product of the electric and magnetic currents exceeds a critical value [50–57]. The instability occurs in the form of long waves, and can produce deformations of the interface sometimes large enough to critically affect the process, including a short circuit in the cell.

Stability analysis of two-fluid layers between electrodes with a small gap but with the Lorenz force aligned tangential to the undisturbed interface is surprisingly scarce, and so is taken to be the subject of the present study. In view of potential applications in microfluidic devices, we focus more on a microscale gap and neglect the gravitational effect. We also exclude complications due to redox reactions, which are sometimes caused in the fluids transported to alleviate corrosion on the electrodes [58]. The results reported here are relevant to studies related to the field-induced flows of liquid metals, for example, in nuclear engineering and cooling systems for electronic devices such as in light-emitting diodes. In these applications, a highly conductive liquid is continuously pumped through the heating-source and heat-sink zones of a micro heat exchanger.

In the present study, we demonstrate that the EMHD flow propelled by the Lorenz force can develop not only the conventional interfacial and shear modes of instabilities but also an EMHD mode of instability owing to the stresses generated by the Lorenz force in the electrically conducting liquid layers. The study shows that this mode exists beyond a threshold value of the applied magnetic field. A parametric study is performed to distinguish the three different instability modes with different combinations of the ratios of density, viscosity, thickness, and electrical conductivity of the transported fluids. In particular, the conditions under which the EMHD mode of instability dominates over the conventional shear and interfacial modes of instabilities are discussed.

The paper is organized as follows. In Sec. II, we present the theoretical formulation of two-fluid EMHD flow; in Sec. III a base-state analysis is carried out. Sec. IV discusses linear stability analysis of the governing equations and boundary conditions leading to the Orr-Sommerfeld (OS) equations; in Sec. V, first a numerical analysis employing the spectral method and then a long-wave asymptotic analysis are shown. Finally some interesting results of consequence are discussed in Sec. VI.

II. THEORETICAL FORMULATION

We consider two fluid layers, denoted by super- or subscript A and B, of constant density ρ_j ($j = A, B$), viscosity μ_j, and electrical conductivity σ_j confined between two electrodes with separation $d_A + d_B$, where d_j represents the individual layer thickness, as shown in Fig. 1. The flow is driven by the x-direction Lorenz force $\mathbf{J}^j \times \mathbf{B}^j$ generated by the interaction between the externally applied current density in the y direction and the magnetic field in the z direction. Here a Cartesian coordinate system (x, y, z) with unit base vectors $(\mathbf{e}_x, \mathbf{e}_y, \mathbf{e}_z)$, is used with the origin fixed at the mean interface ($y = 0$). An electric potential difference ϕ_0, externally imposed between the electrodes, produces the electric current density

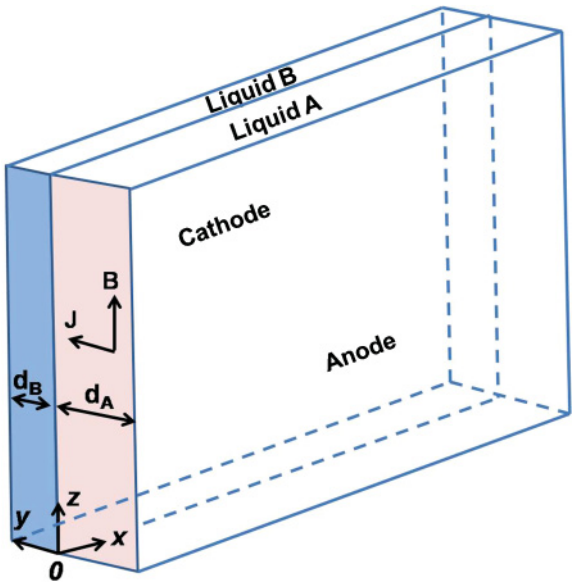

FIG. 1. (Color online) Schematic diagram of x-directional two-layer EMHD flow when subjected to magnetic field in the z direction and an electric field in the y direction.

$$\mathbf{J}^j = \sigma_j(-\nabla\phi^j + \mathbf{u}^j \times \mathbf{B}^j), \tag{2.1}$$

where ϕ is the electric potential, and $\mathbf{u}$ is the velocity vector. The magnetic field is provided by a permanent magnet, and the resulting magnetic flux density is

$$\mathbf{B}^j = Be_z, \tag{2.2}$$

where B is the magnitude of the magnetic flux density imposed. The conservation of mass and momentum for both fluids is expressed by

$$\nabla \cdot \mathbf{u}^j = 0, \tag{2.3}$$

$$\rho_j[\dot{\mathbf{u}}^j + (\mathbf{u}^j \cdot \nabla)\mathbf{u}^j] = -\nabla p^j + \nabla \cdot \bar{\tau}^j + \mathbf{J}^j \times \mathbf{B}^j, \tag{2.4}$$

where $\bar{\tau}^j$, $\mathbf{u}^j\{u^j, v^j\}$, and $p^j$are the stress tensor, velocity vector, and pressure for layer j ($j = A, B$), respectively, and the dot symbol over the velocity vector in Eq. (2.4) represents the time derivative. The conservation law for the current density is written as

$$\nabla \cdot \mathbf{J}^j = \sigma_j \nabla \cdot (-\nabla\phi^j + \mathbf{u}^j \times \mathbf{B}^j) = 0. \tag{2.5}$$

In this study, it is assumed that (i) the magnetic field generated by the electrical current is negligible compared to the imposed magnetic field, (ii) the magnetic diffusion time is much shorter than the period of oscillations, and (iii) the magnetic Reynolds number is negligible. These assumptions help the analysis to remain valid even for liquid metals. No-slip,

impermeability, and constant-potential boundary conditions are applied at the rigid electrodes,

$$\mathbf{u}^A = \mathbf{0} \quad \text{and} \quad \phi^A = \phi_0 \quad \text{at } y = -d_A, \tag{2.6}$$

$$\mathbf{u}^B = \phi^B = 0 \quad \text{at } y = d_B. \tag{2.7}$$

The jump in the normal stress balance and the continuity of tangential stresses and velocities are enforced as boundary conditions at the deformed position of the liquid-liquid interface ($y = h$):

$$(\mathbf{n}\cdot\bar{\boldsymbol{\tau}}^B\cdot\mathbf{n} - \mathbf{n}\cdot\bar{\boldsymbol{\tau}}^A\cdot\mathbf{n} = \gamma\kappa), \tag{2.8}$$

$$(\mathbf{t}\cdot\bar{\boldsymbol{\tau}}^B\cdot\mathbf{n} = \mathbf{t}\cdot\bar{\boldsymbol{\tau}}^A\cdot\mathbf{n}), \tag{2.9}$$

$$(\mathbf{u}^A = \mathbf{u}^B). \tag{2.10}$$

Here the symbols γ and κ represent the surface-tension coefficient and the curvature, respectively. It is assumed that no Marangoni or electromechanical effect is present along the interface. The interfacial boundary conditions for the electric potential are obtained by imposing continuity of the normal component of the current density and the electric potential across the interface ($y = h$):

$$(\mathbf{n}\cdot\mathbf{J^A} = \mathbf{n}\cdot\mathbf{J^B}), \tag{2.11}$$

$$\phi^B = \phi^A. \tag{2.12}$$

Finally the location of the interface ($y = h$) is defined by the kinematic condition,

$$[\dot{h} = -u^j(\partial h/\partial x) + v^j]. \tag{2.13}$$

The symbols $\mathbf{n}\{[-h_x/\sqrt{(1+h_x^2)}, 1/\sqrt{(1+h_x^2)}]\}$ and $\mathbf{t}\{[1/\sqrt{(1+h_x^2)}, h_x/\sqrt{(1+h_x^2)}]\}$ in the boundary conditions represent unit normal and tangent vectors, respectively. The symbols ∇ and ∇_s are the gradient operators. The dimensional governing equations and the boundary conditions [Eqs. (2.1)–(2.13)] are transformed into nondimensional forms by employing the thickness of the layer A (d_A) as length scale and the viscous time scale $\rho_A d_A^2/\mu_A$. The dimensionless variables are then

$$X = x/d_A;\ Y = y/d_A;\ H = h/d_A;\ T = t\mu_A/\rho_A d_A^2;$$

$$\mathbf{U}^j = \mathbf{u}^j\rho_A d_A/\mu_A;\ P^j = p^j\mu_A^2/\rho_A d_A^2;\ \bar{\mathbf{T}}^j = \bar{\tau}^j\mu_A^2/\rho_A d_A^2;$$

$$\Gamma = \rho_A\gamma d_A/\mu_A^2;\ \rho_r = \rho_B/\rho_A;\ \sigma_r = \sigma_B/\sigma_A;\ \mu_r = \mu_B/\mu_A;$$

$$d_r = d_B/d_A;\ \Phi^j = \phi^j/\phi_0;\ E = \rho_A\phi_0/\mu_A B, \text{ and}$$

$$\mathrm{Ha} = d_A B\sqrt{\sigma_A/\mu_A}.$$

The nondimensional forms of the governing equations and boundary conditions are provided in Appendix A. Here the symbol Γ represents the dimensionless surface tension, E is a measure of the electric current imposed, and the Hartmann number (Ha) describes the ratio of Lorenz to viscous force. In the dimensionless form, layers A and B occupy $-1 \leqslant Y \leqslant H$ and $H \leqslant Y \leqslant d_r$, respectively, where $H(X, T)$ is the nondimensional location of the interface between fluids A and B. In what follows all variables and related discussions are given in terms of the nondimensional quantities unless otherwise mentioned.

III. BASE STATE

The two-fluid EMHD flow system described above contains a simple base state of steady unidirectional flow with a plane interface, which is expressed as

$$H = 0,\ \bar{V}^j = \bar{P}^j = 0,\ U^j = \bar{U}^j(Y),\ \text{and}\ \Phi^j = \bar{\Phi}^j(Y)\ \ (j = A, B). \tag{3.1}$$

Here the overbars indicate base-state solutions. The expressions for the steady-state velocity profiles obtained from the governing equations are then

$$\bar{U}^A(Y) = \tfrac{1}{2}\mathrm{Ha}^2 E A_3[(Y^2-1) + A_1(Y+1)], \tag{3.2}$$

$$\bar{U}^B(Y) = \frac{1}{2}\frac{\sigma_r}{\mu_r}\mathrm{Ha}^2 E A_4[(Y^2-d^2) + A_2(Y-d)], \tag{3.3}$$

while those for the steady-state electric potentials are

$$\bar{\Phi}^A(Y) = A_3(Y+1) - \tfrac{1}{2}\mathrm{Ha}^2 A_3\Big[\tfrac{1}{3}(Y^3+1) - (Y+1) + A_1\Big(\tfrac{1}{2}(Y^2-1) + (Y+1)\Big)\Big] + 1, \tag{3.4}$$

$$\bar{\Phi}^B(Y) = A_4(Y-d_r) - \frac{1}{2}\frac{\sigma_r}{\mu_r}\mathrm{Ha}^2 A_4\Big[\frac{1}{3}\big(Y^3-d_r^3\big) - d_r^2(Y-d_r) + A_2\Big(\frac{1}{2}\big(Y^2-d_r^2\big) - d_r\Big(Y-d_r\Big)\Big)\Big], \tag{3.5}$$

where the coefficients (A_i) are evaluated from the boundary conditions on the electrodes and at the interface as

$$A_1 = A_2 = -\frac{d_r^2-\mu_r}{d_r+\mu_r}, \tag{3.6}$$

$$A_3 = \sigma_r A_4 = -\sigma_r \Big/ \left\{d_r + \frac{1}{2}\frac{\sigma_r}{\mu_r}\mathrm{Ha}^2\left(\frac{2d_r^3}{3} + \frac{A_2 d_r^2}{2}\right) + \sigma_r\left[1 - \frac{1}{2}\mathrm{Ha}^2\left(\frac{A_1}{2} - \frac{2}{3}\right)\right]\right\}. \tag{3.7}$$

Both equations (3.2) and (3.4) indicate that the maximum streamwise velocity occurs at the interface for $\mu_r = d_r^2$ and in the interior of either layer otherwise. The base-state velocity profiles ($\bar{U}^j$) and the electric potential ($\bar{\Phi}^j$) with the variations in the viscosity ratio (μ_r), thickness ratio (d_r), and Hartmann number (Ha) are shown in Fig. 2. The broken line in Fig. 2(a) shows that when $\mu_r = d_r = 1$ and $\mathrm{Ha} = 0.05$, the flow profile is parabolic and symmetric with respect to the interface. The solid and the dash-dotted lines in the same plot show that for $\mu_r < 1$ ($\mu_r > 1$) the flow profile becomes asymmetric across the interface with maximum velocity residing in the layer B (layer A). Interestingly, since the applied Lorenz force is a body force, either with increase in volume of the fluid (increasing d_r) or in external field (increasing Ha or E), the velocity of the fluids increases [Figs. 2(b) and 2(c)]. Figure 2(b) shows that the base-state velocity profiles can be asymmetric when the layer thicknesses are unequal ($d_r \neq 1$). An increase in the strength of the external field strength (e.g., increasing Ha) causes an increase in flow in the channel [Fig. 2(c)]. Figure 2(d) shows that electrical properties such as the ratio of the electrical conductivity (σ_r) can also alter the base-state velocity and

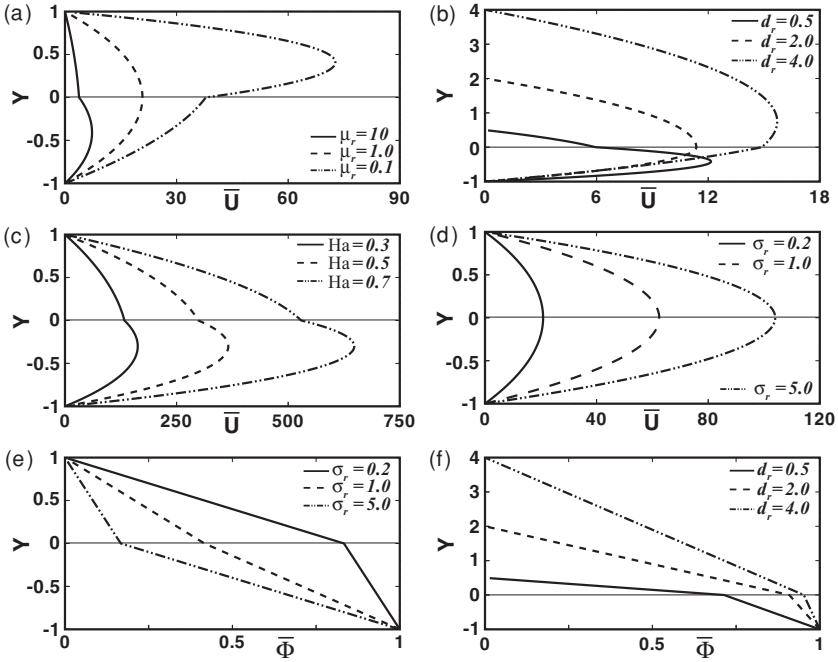

FIG. 2. (a)–(d) Nondimensional base-state velocity ($\bar{U}$) profiles; (e), (f) profiles of the nondimensional potentials ($\bar{\Phi}$) across the width of the channel (Y). In (a) Ha = 0.05, $d_r = 1$, $\sigma_r = 0.2$, in (c) $\mu_r = 4$, $d_r = 1$, $\sigma_r = 0.2$, in (d) Ha = 0.05, $\mu_r = 1$, $d_r = 1$, in (b) and (f) Ha = 0.05, $\mu_r = 4$, $\sigma_r = 0.2$, and in (e) Ha = 0.05, $\mu_r = 4$, $d_r = 1$.

the resulting flow rate. An increase in electrical conductivity stratification at the liquid layers leads to higher flow rate inside the channel. Figures 2(e) and 2(f) depict that, depending upon the physical properties and thicknesses of the liquid layers μ_r, d_r, and σ_r, the gradient of potential varies across the interface in the EMHD flow, which in turn influences the flow rate and eventually the associated flow instabilities.

IV. LINEAR STABILITY ANALYSIS

The nondimensional governing equations (A1)—(A8) and the boundary conditions (A9)—(A16) are linearized by imposing small perturbations to the basic state: $U^j = \bar{U}^j + U'^j$, $V^j = V'^j$, $\Phi^j = \bar{\Phi}^j + \Phi'^j$, and $P^j = \bar{P}^j + P'^j$, where the primes on variables denote small perturbing quantities. The equations for velocity perturbations are then transformed in terms of the stream function (Ψ^j) by using $U'^j = \partial\Psi^j/\partial Y$ and $V'^j = -\partial\Psi^j/\partial X$. The resulting governing equations and the boundary conditions are then linearized by employing normal modes $\Psi^j(X,Y,T) = \tilde{\Psi}^j(Y)e^{iK(X-CT)}$, $P'^j(X,Y,T) = \tilde{P}^j(Y)e^{iK(X-CT)}$, $H(X,Y,T) = \tilde{H}e^{iK(X-CT)}$, and $\Phi'^j(X,Y,T) = \tilde{\Phi}^j(Y)e^{iK(X-CT)}$ to obtain the following dimensionless coupled OS system for layers A and B:

$$(D^2 - K^2)^2\tilde{\Psi}^A = iK(\bar{U}^A - C)(D^2 - K^2)\tilde{\Psi}^A - iK\bar{U}^A_{YY}\tilde{\Psi}^A, \tag{4.1}$$

$$\nu_r(D^2 - K^2)^2\tilde{\Psi}^B = iK(\bar{U}^B - C)(D^2 - K^2)\tilde{\Psi}^B - iK\bar{U}^B_{YY}\tilde{\Psi}^B, \tag{4.2}$$

where D and subscript Y denote d/dY. Here ν_r ($= \mu_r/\rho_r$) is the kinematic viscosity for each fluid, and K and C ($= C_r + iC_i$) represent the wave number and the complex wave speed, respectively. The linearized nondimensional boundary conditions on the electrodes are

$$\tilde{\Psi}^A_Y(-1) = \tilde{\Psi}^A(-1) = \tilde{\Psi}^B_Y(d_r) = \tilde{\Psi}^B(d_r) = 0. \tag{4.3}$$

At the liquid-liquid interface ($Y = 0$),

$$\tilde{P}^B - \tilde{P}^A - 2iK\left(\tilde{\Psi}^A_Y + \tilde{H}\bar{U}^A_Y\right) + 2iK\mu_r\left(\tilde{\Psi}^B_Y + \tilde{H}\bar{U}^B_Y\right) = -K^2\Gamma\tilde{H}, \tag{4.4}$$

$$\left(\tilde{\Psi}^A_{YY} - \mu_r\tilde{\Psi}^B_{YY}\right) + K^2\left(\tilde{\Psi}^A - \mu_r\tilde{\Psi}^A\right) - \left(\bar{U}^A_{YY} - \mu_r\bar{U}^B_{YY}\right)\tilde{H} = 0, \tag{4.5}$$

$$\left(\tilde{\Psi}^A_Y - \tilde{\Psi}^B_Y\right) + \tilde{H}\left(\bar{U}^A_Y - \bar{U}^B_Y\right) = 0, \tag{4.6}$$

$$E\left(\tilde{\Phi}^A_Y - \sigma_r\,\tilde{\Phi}^B_Y\right) + E\tilde{H}\left(\bar{\Phi}^A_{YY} - \sigma_r\,\bar{\Phi}^B_{YY}\right) + \tilde{H}\left(\bar{U}^A_Y - \sigma_r\bar{U}^B_Y\right) + \left(\tilde{\Psi}^A_Y - \sigma_r\,\tilde{\Psi}^B_Y\right) = 0, \tag{4.7}$$

$$\bar{\Phi}^B_Y\tilde{H} + \tilde{\Phi}^B = \bar{\Phi}^A_Y\tilde{H} + \tilde{\Phi}^A, \tag{4.8}$$

$$\tilde{H} = \tilde{\Psi}^A/(C - \bar{U}^A). \tag{4.9}$$

The linearized kinematic condition and further rearrangements yield the following four simpler boundary conditions at the liquid-liquid interface ($Y = 0$):

$$\tilde{\Psi}^A_{YYY} - 3K^2\tilde{\Psi}^A_Y - \mu_r\tilde{\Psi}^B_{YYY} + 3\mu_r K^2\tilde{\Psi}^B_Y + iK\left(C - \bar{U}^A\right)\left[\tilde{\Psi}^A_Y - \rho_r\tilde{\Psi}^B_Y\right] + iK\left[\bar{U}^A_Y\tilde{\Psi}^A - \rho_r\bar{U}^B_Y\tilde{\Psi}^B\right] + \left[\tilde{\Psi}^A/\left(C - \bar{U}^A\right)\right]\left[Ha^2E\left(\bar{\Phi}^A_{YY} - \sigma_r\bar{\Phi}^B_{YY}\right) + Ha^2\left(\bar{U}^A_Y - \sigma_r\bar{U}^A_Y\right) - iK^3\Gamma\right] = 0, \tag{4.10}$$

$$\left[\tilde{\Psi}^A_{YY} + K^2\tilde{\Psi}^A\right] - \mu_r\left[\tilde{\Psi}^B_{YY} + K^2\tilde{\Psi}^B\right] = 0, \tag{4.11}$$

$$\left(\tilde{\Psi}^A_Y - \tilde{\Psi}^B_Y\right) + \left[\tilde{\Psi}^A/(C - \bar{U}^A)\right]\left(\bar{U}^A_Y - \bar{U}^B_Y\right) = 0, \tag{4.12}$$

$$\tilde{\Psi}^A = \tilde{\Psi}^B. \tag{4.13}$$

V. NUMERICAL ANALYSIS

The coupled OS system described above is solved numerically to obtain the linear growth rate (KC_i) and the corresponding wave numbers (K). For this purpose, the D2 algorithm proposed by Dongarra *et al*. [59] for the Chebyshev τ–QZ spectral method [60,61] is employed. The fourth-order OS eigenvalue system is first transformed into second-order ordinary differential equations by introducing two new variables ξ and η as

$$(D^2 - K^2)\tilde{\Psi}^A - \xi = 0, \tag{5.1}$$

$$(D^2 - K^2)\xi + iKC\xi - \frac{1}{2}iKHa^2EA_3\xi[(Y^2-1) + A_1(Y+1)] + iKEHa^2A_3\tilde{\Psi}^A = 0, \tag{5.2}$$

$$(D^2 - K^2)\tilde{\Psi}^B - \eta = 0, \tag{5.3}$$

$$(D^2 - K^2)\eta + \frac{iK}{\nu_r}C\eta - \frac{iK\sigma_r}{2\nu_r\mu_r}Ha^2EA_4[(Y^2-d_r^2) + A_2(Y-d_r)] + \frac{iK\sigma_r}{\nu_r\mu_r}EHa^2A_4\tilde{\Psi}^B = 0. \tag{5.4}$$

The boundary conditions are also transformed in terms of the variables ξ and η to, at the electrodes,

$$\tilde{\Psi}_Y^A(-1) = \tilde{\Psi}^A(-1) = \tilde{\Psi}_Y^B(d_r) = \tilde{\Psi}^B(d_r) = 0, \tag{5.5}$$

and at the liquid-liquid interface,

$$C[\xi - \mu_r\eta + 2K^2(\tilde{\Psi}^A - \mu_r\tilde{\Psi}^B)] - \bar{U}^A[\xi - \mu_r\eta + 2K^2(\tilde{\Psi}^A - \mu_r\tilde{\Psi}^B)] = 0 \tag{5.6}$$

$$C\left(\tilde{\Psi}_Y^A - \tilde{\Psi}_Y^B\right) - \bar{U}^A\left(\tilde{\Psi}_Y^A - \tilde{\Psi}_Y^B\right) + \tilde{\Psi}^A\left(\bar{U}_Y^A - \bar{U}_Y^B\right) = 0, \tag{5.7}$$

$$C^2\left[iK\tilde{\Psi}_Y^A - iK\rho_r\tilde{\Psi}_Y^B\right] + C\left[\left(-2K^2\tilde{\Psi}_Y^A - 2iK\bar{U}^A\tilde{\Psi}_Y^A + iK\bar{U}_Y^A\tilde{\Psi}^A\right) + \xi_Y + \left(2\mu_rK^2\tilde{\Psi}_Y^B + 2iK\rho_r\bar{U}^A\tilde{\Psi}_Y^B - iK\rho_r\bar{U}_Y^B\tilde{\Psi}^B\right) - \mu_r\eta_Y\right] + \left[\begin{array}{l}\left[-iK\bar{U}^A\bar{U}_Y^A + Ha^2E\left(\bar{\Phi}_{YY}^A - \sigma_r\bar{\Phi}_{YY}^B\right) + Ha^2\left(\bar{U}_Y^A - \sigma_r\bar{U}_Y^B\right) - iK^3\Gamma\right]\tilde{\Psi}^A - \bar{U}^A\xi_Y \\ +\left(iK\bar{U}^A\bar{U}^A + 2K^2\bar{U}^A\right)\tilde{\Psi}_Y^A - \left(iK\bar{U}^A\bar{U}^A\rho_r + 2\mu_rK^2\bar{U}^A\right)\tilde{\Psi}_Y^B + iK\bar{U}^A\rho_r\bar{U}_Y^B\tilde{\Psi}^B + \mu_r\bar{U}^A\eta_Y\end{array}\right] = 0. \tag{5.8}$$

The computational domain is then mapped to $(-1,1)$ for each layer by employing the transformation $Z_A = -2Y - 1$ and $Z_B = (2/d_r)Y - 1$, where $Y = -1$ corresponds to the interface and $Y = 1$ corresponds to the bounding electrode for each layer. The resulting differential equations are then expanded in terms of Chebyshev polynomials $T_n(z)$. For N Chebyshev polynomials, we solve for the eigenvalues of a $(4N+8)\times(4N+8)$ matrix, where the remaining eight rows appear from the eight boundary conditions enforced at the electrodes and the interface. For consistency of the results we have varied N between 80 and 120.

A long-wave linear stability analysis of the coupled OS system is also carried out for comparison; it is valid for $K \to 0$. Here $\tilde{\Psi}^A$, $\tilde{\Psi}^B$, C, and H are expanded in power series of K [for example, $\tilde{\Psi}^A = \tilde{\Psi}_0^A + K\tilde{\Psi}_1^A + o(K^2)$, $\tilde{\Psi}^B = \tilde{\Psi}_0^B + K\tilde{\Psi}_1^B + o(K^2)$, $C = C_0 + KC_1 + o(K^2)$, and $H = H_0 + KH_1 + o(K^2)$], and an analysis analogous to that by Yih [17], Pereira and Kalliadasis [62], and Demekhin *et al*. [63] is performed. The details of this long-wave analysis can be found in Appendix B. Following this procedure the first-order correction to the eigenvalue (KC_1) is obtained as

$$C_1 = \frac{iK^3d_r\Gamma}{12(1+d_r)} - \frac{iKHa^2E(\mu_r - d_r^2)[Q_1+Q_2]}{960d_r(1+d_r)^3\nu_r}, \tag{5.9}$$

where the expressions for $Q_1$and $Q_2$are given in Appendix B. It is interesting to note here that as for the PPF the two-layer EMHD flow also exhibits neutral stability (i.e., $C_1 = 0$) for $\mu_r = d_r^2$. According to the expression shown in (5.9) the long-wave instability exists for $\mu_r > d_r^2$. Figure 3 shows the growth rate Ω [a product of the wave number (K)and the imaginary part of the complex wave speed(C_i)] as a function of the wave number (K) obtained from the full OS system employing the spectral method and from the long-wave approximation. In both unstable and stable cases shown in the figure, the viscosity of the less conducting fluid is considered to be higher ($\mu_r = 2$). In the long-wave regime (lower values of K), the two methods are in good agreement. As K increases it is seen that the long-wave analysis overestimates the growth rate. It is important to note in Eq. (5.9) that the surface-tension term appearing at higher order $o(K^3)$ is intentionally retained to show that it does not affect the long-wave analysis, but plays an important role in stabilizing sufficiently short waves.

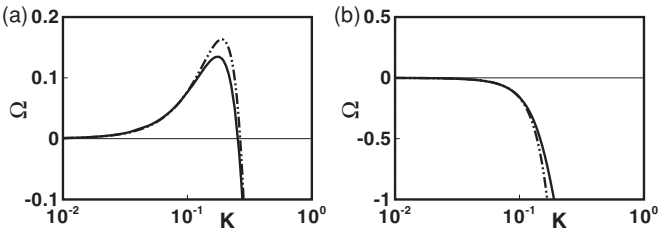

FIG. 3. Comparison of growth rate (Ω) plots from the spectral analysis (solid line) and the long-wave analysis (broken line) for $\mu_r = 2$ and Ha $= 0.05$. (a) $d_r = 0.5$ and (b) $d_r = 2$.

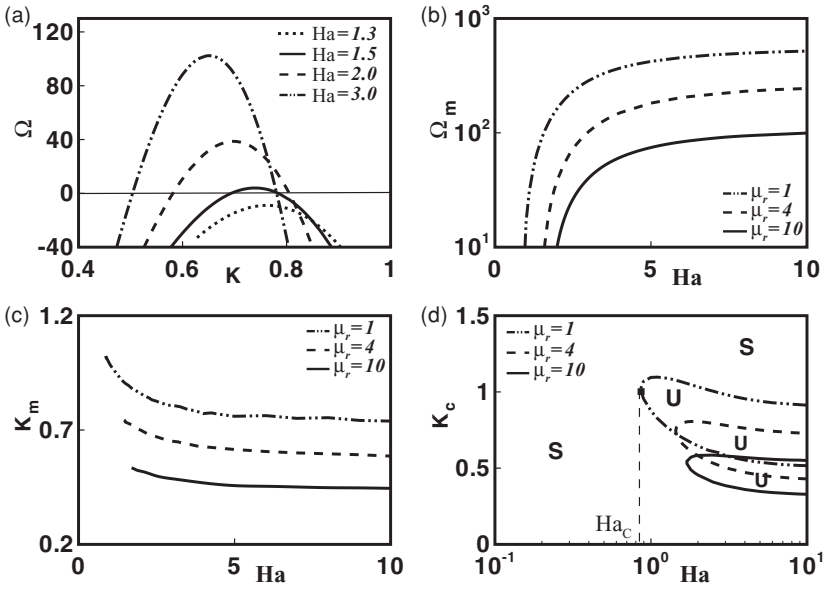

FIG. 4. Influence of electromagnetic field (varying Ha) on neutrally stable mode ($\mu_r = d_r^2$) in two-layer EMHD flow. (a) Growth rate (Ω) curves when $\mu_r = 4$, $d_r = 2$. (b)–(d) Maximum growth rate (Ω_m), dominant wave number (K_m), and neutral stability (K_c) plots, respectively.

VI. RESULTS AND DISCUSSIONS

In view of the preliminary neutral stability condition explained above, we follow the stability-analysis results of conventional pressure-driven channel flows to consider three distinct regimes for ratios of viscosity and thickness of the two layers: (i) $\mu_r > d_r^2$, (ii) $\mu_r < d_r^2$, and (iii) $\mu_r = d_r^2$. Previous studies [17,27,29] show that for pressure-driven flows, the interfacial mode originating from the viscosity stratification dominates when $\mu_r > d_r^2$, the shear mode associated with the Reynolds stresses dominates in the regime $\mu_r < d_r^2$, and the flow is neutrally stable when $\mu_r = d_r^2$. In this section we demonstrate that the EMHD flow encompasses these conventional modes of instabilities and features an entirely different mode of instability beyond a threshold magnetic field strength. Considering that a two-layer EMHD flow is applied to microfluidic devices, we employ the typical magnitudes of dimensional parameters as $\rho_j \sim 1000$ kg/m^3, $\mu_j \sim 0.001$–0.01 Pa s, $\sigma_j \sim 0.1$–4 S/m, $d_j \sim 0.0001$–0.1 m, $\phi_0 \sim 1$ V, $\gamma \sim 0.02$ N/m, and $B \sim 0.01$–10 T. The upper value 4 S/m of the conductivity corresponds to seawater. Liquid metals have much higher conductivities, which make the flow and instabilities even stronger. The flow is driven by the Lorenz force, which is characterized by the Hartmann number Ha, and the range of Ha based on the above parameters is 10^{-3}–10. Modulation of Ha is employed for flow control while maintaining a constant electric field ($E = 10^5$), which results in a dimensional velocity range in the x direction of 10^{-4}–0.1 m/s. As shown by the results discussed below, this magnitude of Ha in microchannels is already sufficient to cause three distinct types of instabilities, including the EMHD instability. Of course, these instabilities are even more readily obtained in macrochannels and with liquid metals. In what follows, unless otherwise mentioned, the results discussed are evaluated employing the dimensionless parameter values $E = 10^5$, $\sigma_r = 0.2$, $\rho_r = 1.0$, and $\gamma = 0.016$ N/m.

We initiate the discussion with the case $\mu_r = d_r^2$, where the interfacial and the shear modes of instabilities are expected to be absent in a two-layer channel flow [17,27,29]. Figure 4(a) shows the variation of the growth rate Ω with the wave number K. Figures 4(b)–4(d) show the variations of the dominant growth rate Ω_m, the dominant wave number (K_m), and the critical wave number K_c of the instability, respectively, with the change in Ha. The dominant growth rate Ω_m signifies the fastest growing unstable mode and is obtained by indentifying the global maxima from the Ω vs K plots. The wave number associated with Ω_m is termed the dominant wave number K_m, which is correlated with the dominant wavelength of instability, Λ_m, by the relation $K_m = 2\pi/\Lambda_m$. The critical wave number K_c is obtained by identifying the neutral stability condition, where the growth rate Ω becomes zero. The dotted line in Fig. 4(a) shows that the two-layer flow is stable when the applied field strength is small (Ha < 1.5) as is expected for any conventional pressure-driven flow under the condition $\mu_r = d_r^2$. For a sufficiently large Ha, however, an instability is exhibited. This is a finite-wave-number EMHD mode absent in conventional pressure-driven flows. Figures 4(b) and 4(c) suggest that this mode of instability grows stronger (increase in Ω_m) as the strength of the external field is increased (increase in Ha), and the instability progressively shifts toward the longer-wavelength regime (decrease in K_m). Figures 4(b) and 4(c) along with the neutral stability diagrams in Fig. 4(d) show that as μ_r and d_r both are increased while maintaining the condition $\mu_r = d_r^2$, the critical value of Ha (Ha$_c$) required to initiate the EMHD instability increases because of the larger viscous resistance provided by the thicker viscous layer. Consequently, the magnitude of the dominant growth rate Ω_m is reduced, and the corresponding wavelength Λ_m increases, as shown in Figs. 4(b) and 4(c). It is important to note here that this EMHD mode produces traveling waves because the eigenvalues C obtained from the numerical computations contain a nonzero real part C_r for nonzero imaginary part C_i. Figure 5 shows that as the external field strength is increased (increase in Ha) the wave speed of the unstable traveling waves increases regardless of μ_r and d_r.

The origin of this EMHD mode can be credited to the stresses generated by the Lorenz force in the electrically conducting liquid layers. Figure 6 shows that when the

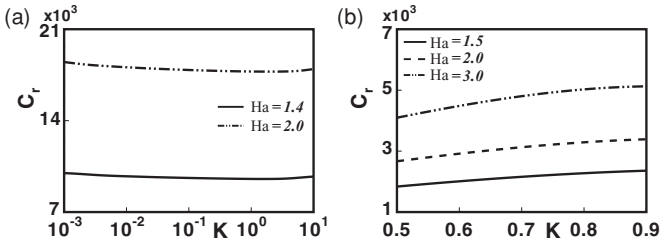

FIG. 5. Influence of electromagnetic field (varying Ha) on real part of wave speed (C_r) in two-layer EMHD flow. (a) $\mu_r = 2, d_r = 1$ $\left(\mu_r > d_r^2\right)$ and (b) $\mu_r = 4, d_r = 2$ $\left(\mu_r = d_r^2\right)$.

condition $\mu_r = d_r = \rho_r = \sigma_r = 1$ (solid line) is satisfied, the EMHD flow is stable when Ha$\sim$ 0.2. However, when $\sigma_r \neq 1$, the EMHD mode of instability appears because of the electrical conductivity stratification at the liquid layers as shown by the broken lines in Fig. 6(a). Figure 2(d) shows that the base flow rate increases with increase in the electrical conductivity stratification. Since the difference in electrical conductivity generates a larger gradient in the Lorenz force across the interface, Fig. 6 shows that for a constant Ha, the dominant growth rate Ω_m increases [Fig. 6(b)] and the dominant wave number K_m decreases [Fig. 6(c)] with the increase in σ_r. The neutral stability plot [Fig. (d)] more clearly shows the appearance of the finite-wave-number EMHD mode when $\sigma_r > 1$ for a fixed Ha. Figures 4 and 6 thus confirm that the force distribution across the interface due to the difference in the stresses originating from the Lorenz force is a major reason for the EMHD mode of instability in two-layer EMHD channel flows.

The EMHD flow also displays the conventional interfacial and the shear modes for low Ha when $\mu_r \neq d_r^2$. The neutral stability plots [Figs. 7(a) and 7(b)] show the effect of μ_r at constant d_r $(= 1)$ and the effect of d_r at constant μ_r $(= 2)$, respectively, for smallHa. The curves in Fig. 7(a) and curves 1(i) $(\rho_r = 1)$ and 2(i) $(\rho_r = 2)$ in Fig. 7(b) all show neutral stability $(C \to 0$ as $K \to 0)$ under the condition $\mu_r = d_r^2$. However, when $\mu_r > d_r^2$, the interfacial mode exists, while the finite-wave-number shear mode exists under the condition $\mu_r < d_r^2$ as shown by the curves 1(ii) and 2(ii) in Fig. 7(b). The broken lines in Fig. 7(b) show the influence of density stratification $(\rho_r = 2)$ on the shear and the interfacial modes. The destabilizing effect of density stratification in two-layer EMHD flows is clearly seen by comparing zones 2(i) and 2(ii) in comparison with the zones 1(i) and 1(ii), where $\rho_r = 1$. Interestingly, at wider electrode separation (high d_r) in EMHD flow, the coupled effect of the viscosity and the density stratification contribute to the enhanced zone of instability, as previously observed for conventional pressure-driven flows [16]. The neutral stability curves shown in Fig. 7(b) for the EMHD flow are also comparable to the similar results obtained for the pressure-driven two-layer PPF under the same flow regime [27]. Figure 7 confirms that at low flow rate (weak external field) the instabilities in a two-layer EMHD channel flow closely mimic the conventional pressure-driven flows at different viscosity, thickness, and density ratios. A comparison between Figs. 4, 6, and 7 also demonstrates that at high external field strength or higher electrical conductivity stratification (higher flow rates) the appearance of the EMHD mode of instability imparts an extra feature to the EMHD flow and the associated instabilities.

The EMHD mode can coexist with the conventional interfacial and shear modes in a two-layer EMHD flow. In Fig. 8, we consider the flow regime $\mu_r > d_r^2$, where the conventional pressure-driven flows show the interfacial mode of instability. Figure 8(a) shows that the long-wave interfacial mode due to viscosity stratification is the only existing instability mode below a threshold value of Ha $(= 2)$ when $\mu_r = 10$ and d_r=3 (solid line 1). At low flow rates the EMHD flow appears similar to pressure-driven flows and so the presence of the long-wave interfacial mode can be justified by the large viscosity stratification when $\mu_r = 10$. As the external field strength is increased, beyond a critical value of Ha, a finite-wave-number instability mode appears (solid line 2). As discussed above, the origin of the EMHD mode can be attributed to the additional stresses due to the Lorenz force generated across the interface of the liquid layers of different

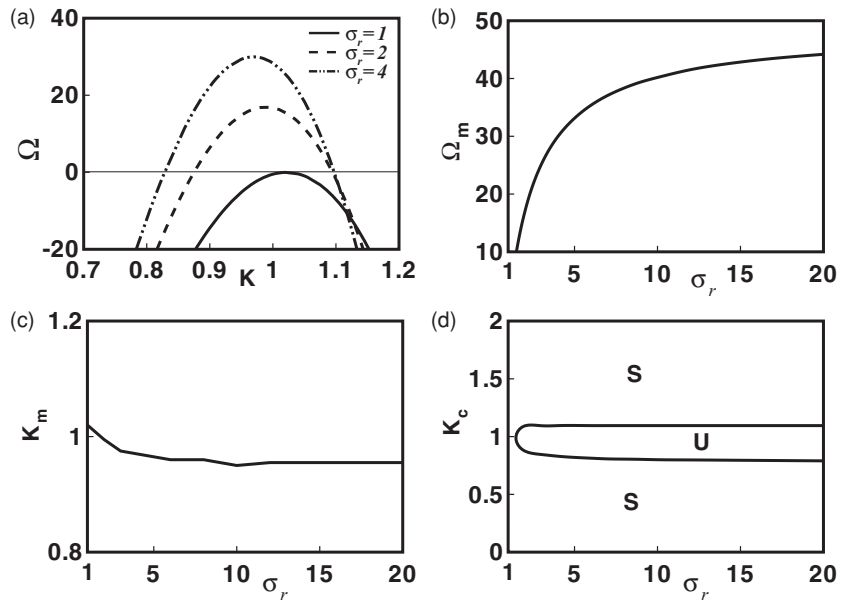

FIG. 6. Influence of σ_r on neutrally stable mode $(\mu_r = d_r^2)$ in two-layer EMHD flow at a constant Ha ($= 0.2$). (a) Growth rate (Ω) curves when $\mu_r = 1, d_r = 1$. (b)–(d) Maximum growth rate (Ω_m), dominant wave number (K_m), and neutral stability (K_c) plots, respectively.

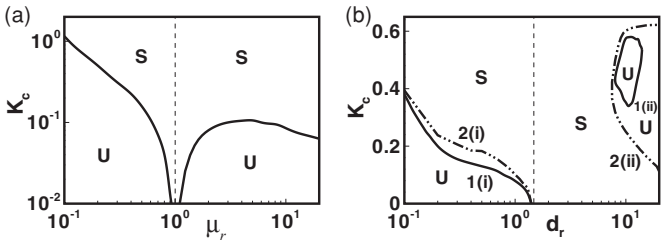

FIG. 7. (a),(b) Neutral stability curves in the (K_c,μ_r) and (K_c,d_r)plane, respectively for the parameter values Ha $= 0.025$ and $\sigma_r = 0.2$. (a) $d_r = 1$, $\rho_r = 1$ and (b) $\mu_r = 2$, $\rho_r = 1$ (solid line) and $\mu_r = 2$, $\rho_r = 2$ (broken line).

electrical conductivity. The solid lines in Figs. 8(a) and 8(b) both show that the growth rate increases with Ha, and both the interfacial and the EMHD modes become more pronounced. For high enough Ha, the EMHD mode becomes the dominant mode of instability. The discontinuity shown by the curve 2 in Fig. 8(c) is associated with the switchover of the dominant mode from the interfacial [curve (i)] to the EMHD mode [curve 2(ii)] at an intermediate wave number. The stability diagrams in Fig. 8(d) more clearly show that the long-wave interface mode is the only existing mode at low Ha and demonstrate the coexistence of the interfacial and the finite-wave-number EMHD modes at higher Ha.

In the regime $\mu_r > d_r^2$ another interesting case is seen for $\mu_r = 3$ and $d_r = 1$. In Fig. 8(a) the curves 3 and 4 show that the interfacial mode can be bimodal in EMHD flows. The bimodality of the interfacial mode in two-layer pressure-driven flow has also been reported previously [27]. The discontinuity in the broken line in Fig. 8(c) is associated with the switching of maxima corresponding to the bimodal interface mode rather than the switchover of instability modes from the interfacial to the EMHD mode. The figure also shows that in this type of two-layer system, the interfacial mode is the dominant mode even at high Ha. The broken line in Fig. 8(d) confirms the existence of the subdominant EMHD mode at high Ha. Figure 8 clearly demonstrates that under the flow regime where $\mu_r > d_r^2$ the EMHD mode can coexist with the interfacial mode. Depending on the strength of the stresses due to the viscosity stratification and the Lorenz force, either mode can be dominant or subdominant.

In the Figs. 9 and 10, we consider the flow regime $\mu_r < d_r^2$, where the finite-wave-number shear mode is the only existing mode in conventional pressure-driven two-layer flows. Figure 9 shows Ω vs K plots under different combinations of μ_r and d_r. When the layers have identical viscosity but different thicknesses ($\mu_r = 1$ and $d_r = 4$), at an intermediate field strength (Ha $= 0.3$ and 0.4) multiple maxima are shown [broken line in Fig. 9(a)], indicating the interference of unstable wave numbers for two different modes. As the value of Ha is increased to 0.5 (solid line), two distinct modes of finite-wave-number instability appear. The larger-wave-number (shorter-wavelength) mode is the conventional shear mode and the smaller-wave-number (longer-wavelength) mode is the EMHD mode. It is important to note here that increase in Ha signifies increase in the strength of the Lorenz force and the flow rate inside the channel. Thus, as the flow rate increases, the shear mode appears, and it shifts toward the shorter-wavelength regime as the flow rate increases. However, the EMHD mode shows a very different behavior. As the field strength increases it shifts toward the longer-wavelength regime. At high Ha (dot-dashed line), the EMHD mode emerges as the only instability mode existing, as the shear mode disappears. When the layers have identical viscosity ($\mu_r = 1$) but different thickness ratio, for example, $d_r = 1$ to $d_r = 10$, the variations of the growth rate of the instability with Ha is observed to be similar, including the changeover of modes. However, when the viscosity of the thicker layer is increased ($\mu_r = 2$ and $d_r = 2$), the viscous resistance suppresses the inertial effects in the thicker layer and the shear mode can be suppressed. Figure 9(b) demonstrates such a case, where the EMHD mode is the only existing instability mode with disappearance of the shear mode. When the thickness of the more viscous layer is increased, the inertial effect again increases as the viscous resistance is reduced. Thus for $\mu_r = 2$ and $d_r = 10$ [Fig. 9(c)], the coexistence of the

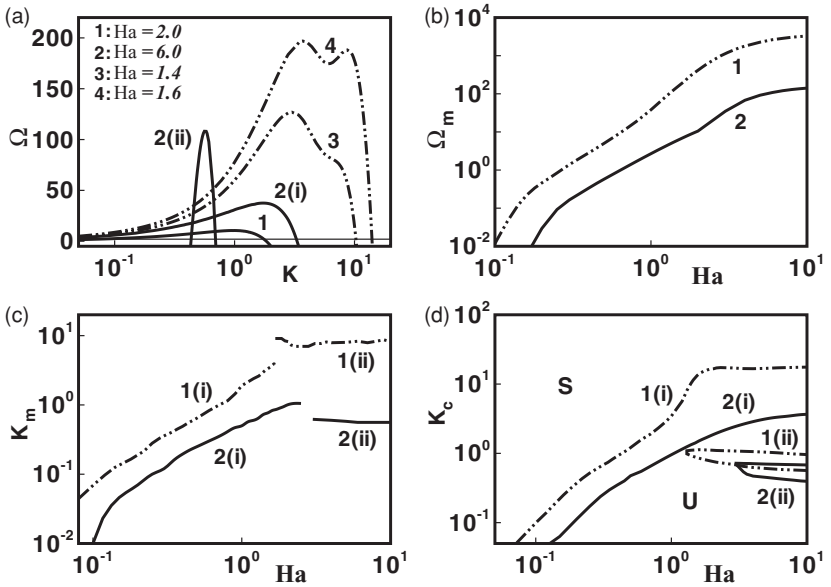

FIG. 8. Influence of electromagnetic field (varying Ha) in two-layer EMHD flow when $\mu_r > d_r^2$. (a) Growth rate (Ω) curves when$\mu_r = 10$, $d_r = 3$. (b)–(d) Maximum growth rate Ω_m, dominant wave number (K_m), and neutral stability (K_c) plots, respectively, when $\mu_r = 2$, $d_r = 1$ (curve 1) and $\mu_r = 10$, $d_r = 3$ (curve 2).

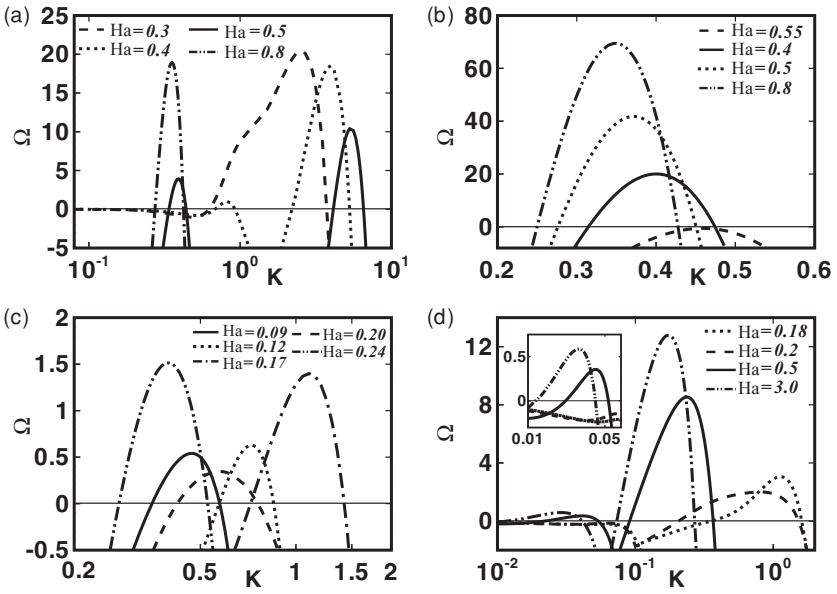

FIG. 9. Influence of electromagnetic field (varying Ha) in two-layer EMHD flow when $\mu_r < d_r^2$. (a)–(d) Growth rate (Ω) curves for $\mu_r = 1$, $d_r = 4$, $\mu_r = 2$, $d_r = 2$, $\mu_r = 2$, $d_r = 10$, and $\mu_r = 2$, $d_r = 20$, respectively.

EMHD and the shear modes is observed. The shear mode dominates below a threshold Ha (<0.17), and with increase in field strength (Ha > 0.24) the EMHD mode dominates over the shear mode. Interestingly, when the thickness of the more viscous layer is very high ($d_r = 20$), a bimodal EMHD mode of instability is observed as Ha is progressively increased. Figure 9(d) shows that at low values of Ha (broken lines) only the shear mode exists. As Ha is increased, an additional subdominant finite-wave-number (see inset) EMHD mode appears with longer wavelength. It shows that, although the growth rates corresponding to both modes grow with Ha, the shorter-wavelength mode is the dominant one even at high Ha. In addition, the wavelength of both modes shifts toward the longer-wavelength regime with increase in Ha. Similar bimodal behavior of the EMHD instability is also observed when the more viscous layer is much thicker, $\mu_r = 4$ and $d_r = 40$, for example (results not shown).

The characteristics of the instabilities shown in Fig. 9 can be more clearly understood from Fig. 10, where Ω_m, K_m, and K_c are plotted against Ha. Figure 10(a) shows the behavior of Ω_m for the cases of $d_r = 4$ and $d_r = 10$ with identical viscosities ($\mu_r = 1$). The two-layer EMHD flow becomes more unstable (increase in Ω_m) with the increase in Ha due to the increasing destabilization arising from the applied Lorenz force. Figure 10(c) shows that at low Ha the short-wave shear mode is the dominant one, and with progressive increase in Ha the instability moves toward the shorter-wavelength regime. However, at intermediate Ha, the EMHD mode is the dominant one and the corresponding wavelength shifts toward the longer-wavelength regime. At intermediate Ha the discontinuities in the Ω_m and K_m plots can be attributed to the switchover from the shear to the EMHD mode of instability. The neutral stability diagrams in Fig. 10(e) show two distinct shorter- (zone a) and longer- (zone b) wavelength regimes, respectively, for the shear and the EMHD modes when $d_r = 4$ (broken line) and $d_r = 10$ (solid line) with $\mu_r = 1$. The disturbances growing due to these two instability modes interfere with each other in zone c. In this zone low flow rates corresponding to low Ha cause these instability modes to interfere and develop a complex phenomenon. The solid lines in Figs. 10(b), 10(d), and 10(f) show a special case, where at very low (high) Ha the shear (EMHD) mode is the dominant mode. At intermediate Ha both modes coexist and interfere with each other. The neutral stability diagram and Fig. 10(b) for K_m show that near the lower-Ha end of this interference zone, the influence of the shear mode is greater, and thus the wave numbers are more shifted toward the shorter-wave-number regime. For a higher Ha the influence of the EMHD mode increases and the instability shifts more toward the longer-wavelength regime. The broken lines in Figs. 10(b), 10(d), and 10(f) show the special case of the bimodal EMHD instability for $\mu_r = 2$ and $d_r = 20$. The dominant mode of the instability grows progressively with Ha, and shifts toward the longer-wavelength regime. The neutral stability diagram clearly demonstrates the existence of two distinct zones of finite wave number for the two different EMHD modes. The dot-dashed line in Figs. 10(b), 10(d), and 10(f) show another special case, where the shear mode is absent and the EMHD mode is the only mode present when $\mu_r < d_r^2$ ($\mu_r = 2$ and $d_r = 2$). As for the other EMHD modes, $\Omega_m$and K_m increases and decreases, respectively, with increasing Ha, and the neutral stability diagrams show a single instability zone at a threshold value of Ha.

In Fig. 11 a stability diagram is illustrated on the Ha_c-d_r plane for different values of μ_r. The critical Hartmann number Ha_c signifies the onset of instability via any of the interfacial, the shear, and the EMHD modes. It is shown that for $\mu_r < d_r^2$ the instability always occurs beyond a critical $\mathrm{Ha} > \mathrm{Ha}_c$. At low Ha the shear mode is dominant. Both the shear and the EMHD modes appear at intermediate Ha, and the EMHD becomes the dominant mode at high Ha. The curves show that Ha_c decays with increase in d_r at a constant μ_r because as the film thickness increases the viscous resistance decreases. However, for a constant d_r, as μ_r is increased, additional viscous resistance requires a larger critical field strength, or Ha_c. The figure also shows that for $\mu_r = d_r^2$ (dot-dashed line), only the EMHD mode is present beyond Ha_c. For $\mu_r > d_r^2$, however, the long-wave interfacial mode is

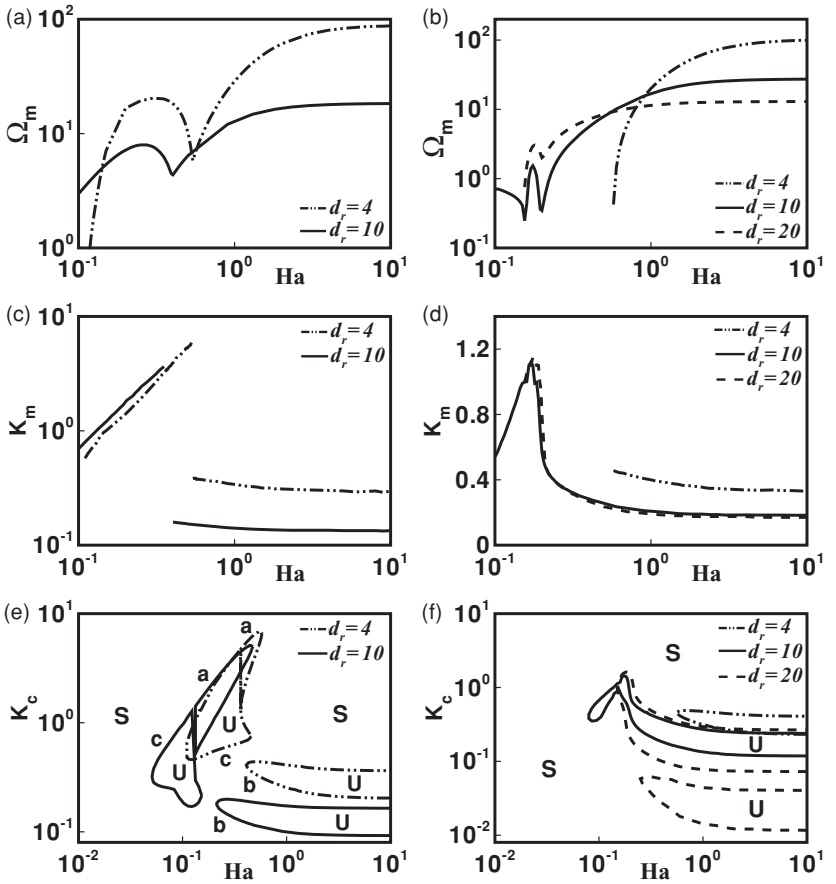

FIG. 10. Influence of electromagnetic field (varying Ha) in two-layer EMHD flow when $\mu_r < d_r^2$. (a) [(b)], (c) [(d)], and (e) [(f)] Maximum growth rate (Ω_m), dominant wave number (K_m), and neutral stability (K_c) plots, respectively, when $\mu_r = 1$ [$\mu_r = 2$].

always unstable for any finite Ha ($\mathrm{Ha}_c = 0$) and coexists with the EMHD mode, which becomes stronger with increasing Ha. The results shown in Fig. 11 can be especially useful for future experiments to be carried out employing two-layer EMHD flow inside rectangular channels. In particular, the theoretical values used for the plots can be used as the starting point in designing the experiments and validating the theoretical results obtained in the present study.

VII. CONCLUSIONS

The EMHD flow and related instabilities of two immiscible layers of electrically conducting Newtonian liquids inside a channel are studied. The EMHD flow is engendered by the Lorenz force, which is enforced by an externally applied electric field acting normally to a magnetic field. A coupled OS system for the two-layer flow is solved numerically employing the spectral method. A long-wave asymptotic analysis on the OS system is also carried out to derive closed-form solutions for the eigenvalues. The results obtained from the spectral method are found to be in good agreement with those from the long-wave analysis especially in the long-wave limit.

The linear stability analysis of the coupled OS system uncovers that the EMHD flow behaves like pressure-driven flows when the applied strength of the Lorenz force is small, and displays the conventional interfacial and shear modes of instability. However, when the external field strength is strong enough the flow develops a finite-wave-number EMHD mode of instability. The shift of the dominant wavelength towards the longer-wavelength regime with progressive increase in the field strength distinguishes the EMHD mode from the conventional shear flow instabilities, which in general show shorter-wavelength instabilities with increasing flow rate. The EMHD mode is also found to appear at lower external field strength when the stratification of the electrical conductivity at the liquid layer is large. Since both greater field strength and larger electrical conductivity stratification at the liquid layers increase the net EMHD flow rate inside the channel, we conclude that the additional stresss at the liquid layers because of the externally applied Lorenz force is the prime reason behind this additional EMHD mode of instability.

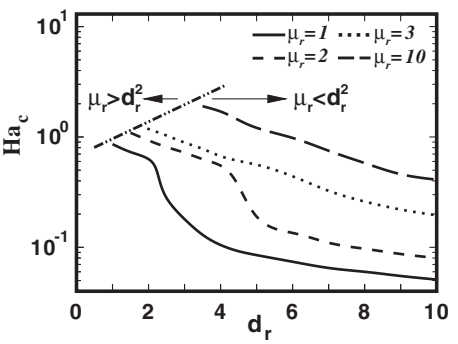

FIG. 11. Critical Hartmann number (Ha_c) plots of the two-layer EMHD flow in the (μ_r,d_r) domain.

The study shows that this mode is more common in two-layer EMHD flows because it persists for all combinations of μ_r and d_r and it is the dominant mode when the external field strength is high (high Ha) or the conductivity stratification is large. It is also shown that, depending on μ_r and d_r of the liquid layers, the EMHD mode of instability can be the only existing mode or can coexist with the interfacial and shear modes of instability in two-layer EMHD flows. The results show that for $\mu_r > d_r^2$ the long-wave interfacial mode is always unstable at any wave number and the EMHD mode can coexist with the former at high field strengths. In contrast, for $\mu_r < d_r^2$, the presence of the finite-wave-number shear mode is observed at low field strengths. At intermediate field strength both shear and EMHD modes coexist and the interference of the unstable wave numbers arising from both the modes can lead to a more complex phenomenon in this EMHD flow regime. However, at high external field strengths the EMHD mode is always the dominant mode of instability in the two-layer EMHD flow. The study also shows that even for $\mu_r = d_r^2$, where the interfacial and the shear modes are absent in the conventional pressure-driven flows, the EMHD mode can persist at higher field strength or at higher electrical conductivity stratification at the liquid layers.

Recent studies indicate that among all the field-driven flows, the EMHD flow has some distinct advantages because of facile control over flow rate, lower energy requirement, and flow reversibility. Thus, the EMHD flow instabilities can be employed to enhance heat and mass transfer, mixing or stirring, and emulsification especially in devices of micro dimensions. Thus, the results discussed in this study of the instability bounds and modes for a wide range of thickness, viscosity, electrical conductivity, and flow rates in two-layer EMHD flow can be of significance when microfluidic or microelectronic devices employing two-layer channel flow are fabricated.

ACKNOWLEDGMENTS

This work was supported by World Class University (WCU) Grant No. R32-2008-000-20082-0 of the Korea Research Foundation. P.D.S.R. and D.B. acknowledge the WCU program for support of their visit to and participation in the WCU Nano Research Center of Yeungnam University. D.B. acknowledges discussions with Gaurav Sharma.

APPENDIX A

The nondimensional continuity equations for the layers are

$$U_X^A + V_Y^A = 0, \tag{A1}$$

$$U_X^B + V_Y^B = 0. \tag{A2}$$

Here subscripts denote partial differentiation. The nondimensional components of the momentum equations for the layer A are

$$\dot{U}^A + U^A U_X^A + V^A U_Y^A = -P_X^A + \left(U_{XX}^A + U_{YY}^A\right) - \mathrm{Ha}^2\left(E\Phi_Y^A + U^A\right), \tag{A3}$$

$$\dot{V}^A + U^A V_X^A + V^A V_Y^A = -P_Y^A + \left(V_{XX}^A + V_{YY}^A\right) + \mathrm{Ha}^2\left(E\Phi_X^A - V^A\right), \tag{A4}$$

and the momentum equations for layer B are

$$\rho_r\left(\dot{U}^B + U^B U_X^B + V^B U_Y^B\right) = -P_X^B + \mu_r\left(U_{XX}^B + U_{YY}^B\right) - \sigma_r \mathrm{Ha}^2\left(E\Phi_Y^B + U^B\right), \tag{A5}$$

$$\rho_r\left(\dot{V}^B + U^B V_X^B + V^B V_Y^B\right) = -P_Y^B + \mu_r\left(V_{XX}^B + V_{YY}^B\right) + \sigma_r \mathrm{Ha}^2\left(E\Phi_X^B - V^B\right). \tag{A6}$$

The governing equations for the electric potentials in the layers A and B are

$$\left(\Phi_{XX}^A + \Phi_{YY}^A\right) + (1/E)\left(U_Y^A - V_X^A\right) = 0, \tag{A7}$$

$$\left(\Phi_{XX}^B + \Phi_{YY}^B\right) + (1/E)\left(U_Y^B - V_X^B\right) = 0. \tag{A8}$$

The nondimensional boundary conditions applied at the anode ($Y = -1$)are

$$U^A = V^A = 0 \text{ and } \Phi^A = 1. \tag{A9}$$

The nondimensional boundary conditions enforced at the cathode ($Y = d_r$) are

$$U^B = V^B = \Phi^B = 0. \tag{A10}$$

The boundary conditions at the deformed position of the liquid-liquid interface ($Y = H$) are

$$P^B - P^A + \frac{2}{\left[1 + H_X^2\right]}\left\{\left[\left(H_X^2 - 1\right)U_X^A - H_X\left(V_X^A + U_Y^A\right)\right] - \mu_r\left[\left(H_X^2 - 1\right)U_X^B - H_X\left(V_X^B + U_Y^B\right)\right]\right\} = \frac{\Gamma H_{XX}}{\left[1 + H_X^2\right]^{3/2}}, \tag{A11}$$

$$\left[\left(U_Y^A + V_X^A\right)\left(1 - H_X^2\right) - 4H_X U_X^A\right] - \mu_r\left[\left(U_Y^B + V_X^B\right)\left(1 - H_X^2\right) - 4H_X U_X^B\right] = 0, \tag{A12}$$

$$U^A = U^B, \tag{A13}$$

$$V^A = V^B, \tag{A14}$$

$$\left(\Phi_Y^A - \Phi_X^A H_X\right) - \sigma_r\left(\Phi_Y^B - \Phi_X^B H_X\right) + \frac{1-\sigma_r}{E}(U^A + H_X V^A) = 0, \tag{A15}$$

$$\Phi^B = \Phi^A. \tag{A16}$$

The nondimensional form of the kinematic equation is

$$\dot{H} = -U^A H_X + V^A = -U^B H_X + V^B. \tag{A17}$$

APPENDIX B

The leading order solution for the stream functions is of the form

$$\tilde{\Psi}_0^A = 1 + B_1 Y + B_2 Y^2 + B_3 Y^3, \tag{B1}$$

$$\tilde{\Psi}_0^B = 1 + B_4 Y + B_5 Y^2 + B_6 Y^3. \tag{B2}$$

The boundary conditions applied to obtain the values of the constants are as follows: At the anode ($Y = -1$),

$$\frac{d\tilde{\Psi}_0^A}{dY} = \tilde{\Psi}_1^A = 0. \tag{B3}$$

At the cathode ($Y = d_r$),

$$\frac{d\tilde{\Psi}_0^B}{dY} = \tilde{\Psi}_0^B = 0, \tag{B4}$$

and at the liquid-liquid interface ($Y = 0$),

$$\tilde{\Psi}_0^A = \tilde{\Psi}_0^B, \tag{B5}$$

$$\left(\frac{d\tilde{\Psi}_0^A}{dY} - \frac{d\tilde{\Psi}_0^B}{dY}\right) + \frac{\tilde{\Psi}_0^A}{C_0'}\left(\frac{d\bar{U}^A}{dY} - \frac{d\bar{U}^B}{dY}\right) = 0, \tag{B6}$$

$$\frac{d^2\tilde{\Psi}_0^A}{dY^2} - \mu_r \frac{d^2\tilde{\Psi}_0^B}{dY^2} = 0, \tag{B7}$$

$$\frac{d^3\tilde{\Psi}_0^A}{dY^3} - \mu_r \frac{d^3\tilde{\Psi}_0^B}{dY^3} + \mathrm{Ha}^2 E\left(\frac{d^2\bar{\Phi}^A}{dY^2} - \sigma_r \frac{d^2\bar{\Phi}^B}{dY^2}\right)\frac{\tilde{\Psi}_0^A}{C_0'} + \mathrm{Ha}^2\left(\frac{d\bar{U}^A}{dY} - \sigma_r \frac{d\bar{U}^B}{dY}\right)\frac{\tilde{\Psi}_0^A}{C_0'} = 0. \tag{B8}$$

Here, the notation $C_0' = \left(C_0 - \bar{U}^A\right)$. The expressions for the constants thus obtained are

$$B_1 = \frac{3d_r^2 + 4d_r^3 + \mu_r}{2d_r^2(1+d_r)}, \quad B_2 = \frac{d_r^3 + \mu_r}{d_r^2(1+d_r)},$$

$$B_3 = -\frac{d_r^2 - \mu_r}{2d_r^2(1+d_r)}, \quad B_4 = -\frac{d_r^3 + 4\mu_r + 3d_r\mu_r}{2d_r(1+d_r)\mu_r},$$

$$B_5 = \frac{d_r^3 + \mu_r}{d_r^2(1+d_r)\mu_r}, \quad B_6 = -\frac{d_r^2 - \mu_r}{2d_r^2(1+d_r)\mu_r}.$$

Employing these constants the following expression for the zeroth-order eigenvalue in the long-wave limit is obtained:

$$C_0 = \frac{\mathrm{Ha}^2 E\left[\left\{-d_r^4 - d_r\mu_r\left(4 + 6d_r + 4d_r^2\right) - \mu_r^2 + \left[d_r^4 + 2d_r\mu_r\left(2 + 2d_r + d_r^2\right) + \mu_r^2\right]A_1\right\}A_3 + 2\left(d_r^2 + d_r^3\right)\sigma_r A_2 A_4\right]}{2\left(d_r^4 + 4d_r\mu_r + 6d_r^2\mu_r + 4d_r^3\mu_r + \mu_r^2\right)}. \tag{B9}$$

The long-wave differential equation with first order terms from the OS equations are

$$\frac{d^4\tilde{\Psi}_1^A}{dY^4} = iK\left[\left(B_{11}Y^2 + B_{12}Y + B_{13} - C_0\right)\frac{d^2\tilde{\Psi}_0^A}{dY^2} - 2B_{11}\tilde{\Psi}_0^A\right], \tag{B10}$$

$$\nu_r \frac{d^4\tilde{\Psi}_1^B}{dY^4} = iK\left[\left(B_{21}Y^2 + B_{22}Y + B_{23} - C_0\right)\frac{d^2\tilde{\Psi}_0^B}{dY^2} - 2B_{21}\tilde{\Psi}_0^B\right]. \tag{B11}$$

Here the notations $B_{11} = \frac{1}{2}\mathrm{Ha}^2 E A_3$, $B_{12} = A_1 B_{11}$, $B_{13} = B_{11}(A_1 - 1)$, $B_{21} = \frac{1}{2}\frac{\sigma_r}{\mu_r}\mathrm{Ha}^2 E A_4$, $B_{22} = A_2 B_{21}$, and $B_{23} = -B_{21}\left(A_2 d_r + d_r^2\right)$. The solutions to Eqs. (B10) and (B11) are

$$\tilde{\Psi}_1^A = B_{A1}Y + B_{A2}Y^2 + B_{A3}Y^3 + iK\left[\frac{B_{11}B_3}{210}Y^7 + \frac{B_{11}B_3}{60}Y^6 + \frac{3B_{13}B_3 + B_{12}B_2 - B_{11}B_1 - 3C_0B_3}{60}Y^5 - \frac{B_{11} + C_0B_2 - B_{13}B_3}{12}Y^4\right], \tag{B12}$$

$$\tilde{\Psi}_1^B = B_{A4}Y + B_{A5}Y^2 + B_{A6}Y^3 + \frac{iK}{\nu_r}\left[\frac{B_{21}B_6}{210}Y^7 + \frac{B_{22}B_6}{60}Y^6 + \frac{3B_{23}B_6 + B_{22}B_5 - B_{21}B_4 - 3C_0B_6}{60}Y^5 - \frac{B_{21} + C_0B_5 - B_{23}B_6}{12}Y^4\right]. \tag{B13}$$

The coefficients are solved from the following first-order boundary conditions:At the anode ($Y = -1$),

$$\frac{d\tilde{\Psi}_1^A}{dY} = \tilde{\Psi}_1^A = 0. \tag{B14}$$

At the cathode ($Y = d_r$),

$$\frac{d\tilde{\Psi}_1^B}{dY} = \tilde{\Psi}_1^B = 0. \tag{B15}$$

And at the interface ($Y = 0$),

$$\tilde{\Psi}_1^A = \tilde{\Psi}_1^B, \tag{B16}$$

$$\left(\frac{d\tilde{\Psi}_1^A}{dY} - \frac{d\tilde{\Psi}_1^B}{dY}\right) - \frac{C_1\tilde{\Psi}_0^A}{C_0'^2}\left(\frac{d\bar{U}^A}{dY} - \frac{d\bar{U}^B}{dY}\right) = 0, \tag{B17}$$

$$\frac{d^2\tilde{\Psi}_1^A}{dY^2} - \mu_r\frac{d^2\tilde{\Psi}_1^B}{dY^2} = 0, \tag{B18}$$

$$\frac{\partial^3\tilde{\Psi}_1^A}{\partial Y^3} - \mu_r\frac{\partial^3\tilde{\Psi}_1^B}{\partial Y^3} + iKC_0'\left[\frac{\partial\tilde{\Psi}_0^A}{\partial Y} - \rho_r\frac{\partial\tilde{\Psi}_0^B}{\partial Y}\right] + iK\left[\frac{\partial\bar{U}^A}{\partial Y}\tilde{\Psi}_0^A - \rho_r\frac{\partial\bar{U}^B}{\partial Y}\tilde{\Psi}_0^B\right] - \mathrm{Ha}^2\left[E\left(\frac{\partial^2\bar{\Phi}^A}{\partial Y^2} - \sigma_r\frac{\partial^2\bar{\Phi}^B}{\partial Y^2}\right) + \left(\frac{\partial\bar{U}^A}{\partial Y} - \sigma_r\frac{\partial\bar{U}^B}{\partial Y}\right)\right] \times \frac{C_1\tilde{\Psi}_0^A}{C_0'^2} - iK^3\Gamma\frac{\tilde{\Psi}_0^A}{C_0'} = 0. \tag{B19}$$

The eigenvalue obtained from the first-order polynomials has the following form:

$$C_1 = \frac{iK^3d\Gamma}{12(1+d_r)} - \frac{iK\mathrm{Ha}^2E(\mu - d^2)[Q_1 + Q_2]}{960d_r(1+d_r)^3\nu_r}. \tag{B20}$$

Here the following notations are used:

$$Q_1 = \mathrm{Ha}^2E\frac{(\sigma_rA_4)^2\left(d_r^2-1\right)\left(d_r+d_r^2\right)}{\mu_r(\mu_r+d_r)}\left\{\left[-10\left(A_2d_r + d_r^2\right)d_r + 3A_2d_r^2 - 4d_r^3\right] - \mu_r\nu_r(4 - 7A_1 + 10) + 10\mu_r(d_r + \nu_r)\right\},$$
$$Q_2 = 5\mathrm{Ha}^2E\left(\frac{\sigma_rA_4}{\mu_r+d_r}\right)^2\left\{[d_r + \nu_r(-1 + 2\rho_r)] - d_r^3\left[d_r^2 + d_r(2 + \nu_r) + 2\mu_r\right] + 2d_r[\mu_r + d_r(1 + \nu_r - \mu_r)]\right\}. \tag{B21}$$

[1] W. Ritchie, Philos. Trans. R. Soc. London **122**, 279 (1832).
[2] J. Jang and S. S. Lee, Sens. Actuators **80**, 84 (2000).
[3] A. V. Lemoff and A. P. Lee, Sens. Actuators, B **63**, 178 (2000).
[4] H. H. Bau, J. Zhong, and M. Yi, Sens. Actuators, B **79**, 207 (2001).
[5] H. H. Bau, J. Z. Zhu, S. Qian, and Y. Xiang, Sens. Actuators, B **88**, 205 (2003).
[6] H. Kabbani, M. Marc, S. W. Joo, and S. Qian, J. Fluids Eng. **130**, 091204 (2008).
[7] J. Zhong, M. Yi, and H. H. Bau, Sens. Actuators **96**, 59 (2002).
[8] B. West, B. Karamata, B. Lillis, J. P. Gleeson, and J. K. Alderman, Lab Chip **2**, 224 (2002).
[9] J. P. Gleeson, O. M. Roche, J. West, and A. Gelb, SIAM J. Appl. Math. **64**, 1294 (2004).
[10] M. Yi, S. Qian, and H. H. Bau, J. Fluid Mech. **468**, 153 (2002).
[11] S. Qian, J. Z. Zhu, and H. H. Bau, Phys. Fluids **14**, 3584 (2002).
[12] S. Qian and H. H. Bau, Mech. Res. Commun. **36**, 10 (2009).
[13] M. C. Weston, M. D. Gerner, and I. Fritsch, Anal. Chem. **82**, 3411 (2010).
[14] D. D. Joseph and Y. Y. Renardy, *Fundamentals of Two-Fluid Dynamics, Part I: Mathematical Theory and Applications* (Springer, Berlin, 1993).
[15] K. P. Chen, Appl. Mech. Rev. **48**, 763 (1995).
[16] P. A. M. Boomkamp and R. H. M. Miesen, Int. J. Multiphase Flow **22**, 67 (1996).
[17] C. -S. Yih, J. Fluid Mech. **27**, 337 (1967).
[18] C. E. Hickox, Phys. Fluids **14**, 251 (1971).
[19] M. K. Smith and S. H. Davis, J. Fluid Mech. **121**, 187 (1982).
[20] A. P. Hooper, Phys. Fluids **28**, 1613 (1985).
[21] D. D. Joseph, M. Renardy, and Y. Y. Renardy, J. Fluid. Mech. **141**, 309 (1984).
[22] Y. Y. Renardy, Phys. Fluids **28**, 3441 (1985).
[23] Y. Y. Renardy, Phys. Fluids **30**, 1627 (1987).
[24] A. P. Hooper and W. G. C. Boyd, J. Fluid Mech. **128**, 507 (1983).
[25] P. G. Drazin, and W. H. Reid, *Hydrodynamic Stability* (Cambridge University Press, London, 1981).
[26] A. P. Hooper and W. G. C. Boyd, J. Fluid Mech. **179**, 201 (1987).
[27] S. G. Yiantsios, and B. G. Higgins, Phys. Fluids **31**, 3225 (1988).
[28] T. W. Kao and C. Park, J. Fluid Mech. **52**, 401 (1972).
[29] A. P. Hooper, Phys. Fluids A **1**, 1133 (1989).
[30] J. R. Melcher, *Field-Coupled Surface Waves: A Comparative Study of Surface-Coupled Electrohydrodynamic and Magnetohydrodynamic Systems* (MIT Press, Cambridge, MA, 1963).

[31] A. Mohamed, E. F. Elshehawey, and M. F. ElSayed, J. Colloid Interface Sci. **169**, 65 (1995).
[32] D. T. Papageorgiou and P. G. Petropoulos, J. Eng. Math. **50**, 223 (2004).
[33] O. Ozen, N. Aubry, D. T. Papageorgiou, and P. G. Petropoulos, Phys. Rev. Lett. **96**, 144501 (2006).
[34] O. Ozen, N. Aubry, D. T. Papageorgiou, and P. G. Petropoulos, J. Fluid Mech. **583**, 347 (2007).
[35] R. V. Craster and O. K. Matar, Phys. Fluids **17**, 032104 (2005).
[36] K. John, P. Hänggi, and U. Thiele, Soft Matter **4**, 1183 (2008).
[37] S. A. Roberts and S. Kumar, J. Fluid Mech. **631**, 255 (2009).
[38] D. Bandyopadhyay, A. Sharma, U. Thiele, and P. D. S. Reddy, Langmuir **25**, 9108 (2009).
[39] S. Chandrasekhar, *Hydrodynamic and Hydromagnetic Stability* (Oxford University Press, New York, 1981).
[40] P. A. Davidson, *An Introduction to Magnetohydrodynamics* (Cambridge University Press, Cambridge, 2001).
[41] N. Gordeev and V. V. Murzenko, Appl. Math. Theor. Phys. **3**, 96 (1990).
[42] S. Korsunsky, Eur. J. Mech. B/Fluids **18**, 295 (1999).
[43] P. Tso and K. Sundaravadivelu, J. Phys. D **34**, 3522 (2001).
[44] P. Yecko, Phys. Fluids **21**, 034102 (2009).
[45] P. Yecko, Phys. Fluids **22**, 022103 (2010).
[46] A. Brask, G. Goranovic, M. J. Jensen, and H. Bruus, J. Micromech. Microeng. **15**, 883 (2005).
[47] Y. Gao, C. Wang, T. N. Wong, C. Yang, N. Y. Nguyen, and K. T. Ooi, J. Micromech. Microeng. **17**, 358 (2007).
[48] S. Qian, S. W. Joo, Y. Jiang, and M. A. Cheney, Mech. Res. Commun. **36**, 82 (2008).
[49] W. S. Choi, A. Sharma, S. Qian, G. Lim, and S. W. Joo, J. Colloid Interface Sci. **347**, 153 (2010).
[50] V. Bojarevics and M. V. Romerio, Eur. J. Mech. B/Fluids **13**, 33 (1994).
[51] A. D. Sneyd and A. Wang, J. Fluid Mech. **263**, 343 (1994).
[52] P. A. Davidson and R. I. Lindsay, J. Fluid Mech. **362**, 273 (1998).
[53] A. Lukyanov, G. El, and S. Molokov, Phys. Lett. A **290**, 165 (2001).
[54] J. S. Morris and P. A. Davidson, J. Fluid Mech. **493**, 121 (2003).
[55] D. Munger and A. Vincent, J. Comput. Phys. **217**, 295 (2006).
[56] H. Kohno and S. Molokov, Phys. Lett. A **366**, 600 (2007).
[57] H. Kohno and S. Molokov, Int. J. Eng. Sci. **45**, 644 (2007).
[58] S. Qian and H. H. Bau, Sens. Actuators, B **106**, 859 (2005).
[59] J. J. Dongarra, B. Straughan, and D. W. Walker, Appl. Numer. Math. **22**, 399 (1996).
[60] S. A. Orszag, J. Fluid Mech. **50**, 689 (1971).
[61] D. Gottlieb and S. A. Orszag, *Numerical Analysis of Spectral Methods: Theory and Applications,* CBMS Conference Series in Applied Mathematics (Capital City Press, Montpelier, Vermont, U.S.A., 1977).
[62] A. Pereira and S. Kalliadasis, Phys. Rev. E **78**, 036312 (2008).
[63] E. A. Demekhin, S. Kalliadasis, and M. G. Velarde, Phys. Fluids **18**, 042111 (2006).